Application of Bayesian optimization for the synchrotron slow extraction tuning*

Ze-Jiang Wang,[1,2,3] Hong-Juan Yao,[1,2,3] Xiao-Yu Liu,[1,2,3] Wen-Bo Ye,[4] Yang Xiong,[1,2,3] Shu-Xin Zheng,[1,2,3,†] Mao-Cheng Wang,[4] Di Wang,[4] Min-Wen Wang,[4] Ye Yang,[4] Wo-Long Liu,[4] Ming-Tong Zhao,[4] Yi-Hua Yan,[4] and Zhong-Ming Wang[4]

[1]Key Laboratory of Particle and Radiation Imaging (Tsinghua University), Ministry of Education, Beijing 100084, China
[2]Laboratory for Advanced Radiation Sources and Application, Tsinghua University, Beijing 100084, China
[3]Department of Engineering Physics, Tsinghua University, Beijing 100084, China
[4]National Key Laboratory of Intense Pulsed Radiation Simulation and Effect (Northwest Institute of Nuclear Technology), Xi'an, 710024, China

We examine the potential of Bayesian optimization for the slow extraction tuning process. In particular, two scenarios are focused on: single energy extraction below the third-order resonance and multiple-energy extraction. At the Xi'an Proton Application Facility synchrotron, low energy slow extraction is adversely affected by the strong space charge effect. The horizontal tune is set below the third order resonance to avoid the large tune shift influence. However, changing the sign of the tune distance flips the slow extraction separatrix distribution in phase space, reducing the extraction efficiency. A high extraction efficiency setting was obtained by parameters scanning in conjunction with operator's experience, but this process is time-consuming. We describe the implementation of Bayesian optimization and show the results in simulation and a proof of principle experiment. Results demonstrate that Bayesian optimization can speed up the tuning procedure while ensuring high quality of the resulting solution. Furthermore, the application of this method in multiple-energy extraction is described and validated only by simulation. In the context of multiple-energy extraction, the objective of optimization is not only to improve the extraction efficiency of an energy step but also to control the area of the stable phase region. To address this multi-objective optimization challenge, the concept of extraction intensity overshoot is used as a proxy for the area of the stable region, while the extraction bump orbit position and angle are incorporated into the optimization parameters. By condensing the two objectives into a single figure of merit, the optimization objective can be reached with Bayesian optimization.

Keywords: Bayesian optimization, Synchrotron, Slow extraction, Beam commissioning

I. INTRODUCTION

Synchrotrons utilizing third-order resonance slow extraction techniques have a wide range of applications, including in the fields of nuclear physics [1–3], radiation therapy [4–8] and space radiation environment simulation [9–11]. In order to achieve the slow extraction of particles, a number of components are required to perform a variety of functions. These functions include control of the tune, resonance excitation and creation of extraction bump orbit. Currently, the theory guiding the design of slow extraction system is well-established [5, 12]. By measuring and correcting relevant extraction parameters to approach the designed values, a relatively high extraction efficiency can often be achieved.

However, beam dynamics are influenced by numerous non-linearly correlated parameters and are subject to some physical phenomena. In some specific cases, the third-order resonance slow-extraction tuning also encounters some problems that increase the time required for tuning. For example, low-energy proton beams are more affected by space-charge effect due to their low energy. A strong space charge effect can result in a substantial incoherent tune shift [13]. To address such influence on the slow extraction tuning of a 10 MeV proton beam, Y. Yang [14] employed a strategy of positioning the horizontal tune below the third-order resonance. The typical extraction horizontal tune value is about 1.661, which is less than 5/3. The change in tune brings a phase-space flipping that makes some original extraction parameters design experience above 5/3 no longer valid.

At XiPAF, experiments have been conducted to improve the efficiency of the extraction process at 10 MeV by Y. Yang, and the extraction efficiency was optimized to exceed 65%. However, the manual optimization of the extraction efficiency is a time-consuming process. In this context, manual optimization refers to the parameters scanning in conjunction with operator's experience.

The technique of Multiple-energy extraction (MEE) technique was originally developed and demonstrated at the Heavy Ion Medical Accelerator in Chiba (HIMAC), uses incremental beam deceleration to deliver multiple discrete energies within a single accelerator cycle [15, 16]. At HIMAC, the number of energy steps is 202 and the range interval is 1-2 mm water-equivalent length [17]. To increase the extraction efficiency, it is reported that some parameters such as the quadrupole magnet current and the bump orbit have to be adjusted [18]. In Yamagata University, the number of energy steps in-

* Supported by National Natural Science Foundation of China (No. 12075131)

† Corresponding author, zhengsx@tsinghua.edu.cn

creases to 600 for 0.5 mm water-equivalent length step in order to eliminate the range shifter[19]. Nevertheless, the extraction efficiencies from 600 energy steps are approximately 20 to 70 percent, indicating a potential for improvement[20]. Accordingly, a future objective is to optimize the tune with the aim of enhancing the extraction efficiency[20]. Therefore, optimizing extraction parameters for hundreds of discrete energies in medical synchrotrons within a limited time-frame also presents considerable difficulties.

Additionally, accelerators are susceptible to both short-term and long-term drifts, necessitating regular parameter adjustments to ensure optimal performance. Therefore, a fast beam tuning optimization method is to be expected.

The use of model-independent optimizers has been demonstrated to be an effective approach for automating the tuning process. This is evidenced by the successful implementation of such methods as the simplex algorithm [21–23], extremum seeking [24–26], and robust conjugate direction search [27, 28]. Nevertheless, these methods frequently necessitate a considerable number of costly evaluations and can get stuck in local optima.

Recently, Bayesian optimization (BO), a class of algorithms, has gained prominence in the accelerator field. It is noteworthy that BO has been successfully applied at facilities such as the Linac Coherent Light Source (LCLS) [29, 30] and SwissFEL [31] for tuning free-electron lasers, thereby encouraging its application for other accelerator tuning tasks [32–34]. A comprehensive review of BO applications in accelerator physics can be found in Ref. [35].

Bayesian optimization (BO) is an iterative, model-based algorithm that excels in the efficient optimization of noisy and costly black-box functions [36–38]. This efficiency is achieved through the application of Bayes' theorem, which incorporates prior knowledge and information from previous steps to maximize the value of each new measurement. BO has been demonstrated to outperform other methods [39].

The process of slow beam extraction can be considered a black-box function optimization problem, which makes BO a suitable method for the extraction tuning process. Xi'an Proton Application Facility (XiPAF) synchrotron is a 10∼200 MeV proton ring of 30.9 m circumference and it serves as a testbed for this study. In this article, we present the application of BO in two scenarios of the slow extraction process. Firstly, we examine the application of BO to the single energy slow extraction (SEE) below the resonance with simulations and a proof-of-principle experiment. Due to time constraints, only two runs were tested in the experiment. Secondly, we investigate the application of BO to MEE in simulation. In contrast to SEE, the objective of MEE is to enhance the overall efficiency across all energy steps. A detailed account of MEE can be found in Sec. IV. The two cases demonstrate the applicability and efficacy of BO in achieving fast and robust slow extraction optimization.

II. BAYESIAN OPTIMIZATION AND THE APPLICATION BACKGROUND

A. Bayesian optimization

In general, BO consists of three main steps, as illustrated in Algorithm 1 [38]. Firstly, BO employs a statistical surrogate model of the objective function, f. This is typically constructed using a Gaussian process (GP) [40]. This approach is based on the assumption that the objective function, f, is drawn from a prior probability distribution, $p(A)$. Following the initialization and observation of $f(\mathbf{x})$, the posterior distribution, $p[A|f(\mathbf{x})]$, is constructed in accordance with Bayes' theorem.

$$p[A|f(\mathbf{x})] \propto p[f(\mathbf{x})|A]p(A). \tag{1}$$

The second step is to define an acquisition function $\alpha(\mathbf{x})$ based on the GP model, which defines the next point to be evaluated. The final step solves for the point (or set of points) that maximizes the acquisition function and thus is predicted to provide the most value towards the optimization objectives. This process is repeated until an optimization criterion is met or a specified number of evaluations is reached.

Algorithm 1 Bayesian Optimization Process

1. Specify the prior distribution for the GP.
2. Collect initial observations of the objective function f at n_0 starting points to form the initial dataset D_0.
3. **for** $t = 1, 2, \ldots$ **do**
4. Update the GP model using the accumulated data D_{t-1}.
5. Determine the next evaluation point $\mathbf{x}_t = \arg\max_a \alpha(\mathbf{x}|D_{t-1})$.
6. Observe y_t at point $\mathbf{x}_t$.
7. Expand the dataset $D_t = D_{t-1} \cup (\mathbf{x}_t, y_t)$.
8. **end for**

1. Gaussian process

A GP model is a distribution of possible functions

$$f(\mathbf{x}) \sim \mathrm{GP}\left[\mu(\mathbf{x}), k(\mathbf{x}, \mathbf{x}')\right] \tag{2}$$

where $\mu(\mathbf{x})$ is referred to as the prior mean function and $k(\mathbf{x}, \mathbf{x}')$ is commonly referred to as the covariance kernel function. To simplify calculations, the prior mean function is given as $\mu(\mathbf{x}) = 0$, which is commonly used when the shape of the objective function is unknown.

The covariance function $k(\mathbf{x}, \mathbf{x}')$, also known as the kernel, describes the similarity between data points. In this study, we use the Matérn kernel [41, 42] and it is defined as:

$$k_{MA}(\mathbf{x}, \mathbf{x}') = \frac{2^{1-\nu}}{\Gamma(\nu)} \left(\sqrt{2\nu}d/l\right)^{\nu} K_{\nu}\left(\sqrt{2\nu}d/l\right). \tag{3}$$

Where $d = ||\mathbf{x} - \mathbf{x}'||$ is the Euclidean distance between the inputs, Γ is the gamma function, and K_ν is the modified Bessel function of the second kind. The length scale of the kernel is denoted by l, and ν controls the smoothness of the resulting function. The Matérn kernel with $\nu = 2.5$ is often used as a starting point for modeling physical functions in the absence of prior information [35].

To emulate the noise present in the real observed signal, a Gaussian distributed noise is added to the covariance function as diagonal terms. Thus, the kernel becomes

$$k(\mathbf{x}, \mathbf{x}') = \sigma^2 k_{MA}(\mathbf{x}, \mathbf{x}') + \sigma^2_{noise} I. \tag{4}$$

The covariance function amplitude σ^2, the noise variance σ^2_{noise}, and the length scale l are referred to as the hyper-parameters, that determine the behavior of the GP.

The noise variance σ^2_{noise} is added to the diagonal of the kernel matrix during fitting. This can prevent a potential numerical problem during fitting, by ensuring that the calculated values form a positive definite matrix. It can also be interpreted as the variance of additional Gaussian measurement noise on the training observations. Therefore, the noise level can be determined by measuring the fluctuation of the objective function.

Since there is no dedicated optimization data stored in the database, the length scale l and the covariance function amplitude σ^2 are learned from training data collected during optimization. A common strategy for learning the hyper-parameters from experimental data is maximizing the marginal log-likelihood (MLL) of the GP model with respect to the hyperparameter values.

In this study, we use the Matérn kernal with its parameter ν set to 2.5. Other hyper-parameters are determined as explained above. The GP model building and regression is realized by the Scikit-learn library [43].

2. Acquisition function

With a GP model that infers the posterior distribution of the objective function, an acquisition function $\alpha(\mathbf{x})$ is constructed to guide the search for the optimum. Maximizing the acquisition function is used to select the next point at which to evaluate the function. That is, we want to sample f at $\mathrm{argmax}_x\ \alpha(\mathbf{x}|D)$.

We use two different acquisition functions in this study: the upper confidence bound (UCB) and the expected improvement (EI). The UCB acquisition function [44] is constructed from the GP prediction mean and standard deviation

$$\alpha_{UCB}(\mathbf{x}) = \mu(\mathbf{x}) + \kappa\sigma(\mathbf{x}), \tag{5}$$

where $\mu(\mathbf{x})$ and $\sigma(\mathbf{x})$ are the GP posterior mean and standard deviation, the parameter κ controls the exploration-exploitation trade-off. Defining UCB with a larger κ value favors exploration, while smaller values of κ prioritize exploitation.

The EI acquisition function calculates the expected value of the improvement of a proposed point $\mathbf{x}$ over the best observed value f_{best} [45]

$$\begin{aligned} \alpha_{EI}(\mathbf{x}) &= \mathbb{E}[\max(f(\mathbf{x}) - (f_{best} + \xi), 0)] \\ &= (\mu(\mathbf{x}) - (f_{best} + \xi))\Phi(Z) + \sigma(\mathbf{x})\phi(Z) \\ Z &= (\mu(\mathbf{x}) - (f_{best} + \xi))/\sigma(\mathbf{x}), \end{aligned} \tag{6}$$

where Φ and ϕ denote the Cumulative Density Function (CDF) and Probability Density Function (PDF) of a normal distribution. The exploration-exploitation trade-off in EI is determined by a positive parameter ξ. In general, higher values of ξ lead to more exploration.

The BO package implemented in this study is based on an open source constrained global optimization tool [46]. Scipy [47] functionalities are used to maximize the acquisition functions.

B. Application background

XiPAF is the first facility in China dedicated to simulate the space radiation environment [10, 48, 49]. It is consisted of a 7 MeV linac injector and a compact synchrotron. The XiPAF synchrotron is a 10∼200 MeV proton ring of 30.9 m circumference. The layout of the XiPAF synchrotron is shown in Fig. 1.

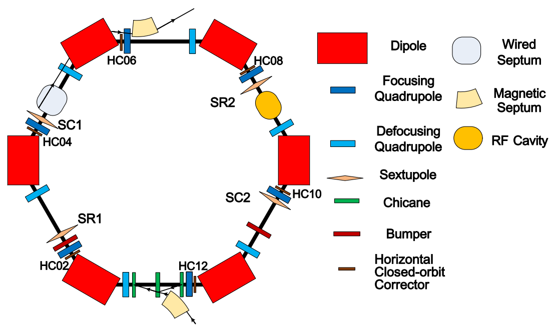

Fig. 1. Scheme of the XiPAF synchrotron layout.

During irradiation, the beam is slowly and continuously extracted by third-order resonance slow extraction. This is achieved by setting the horizontal tune close to the third-order resonance which for XiPAF is 5/3 and turning on the resonant sextupole magnets (SR). Then a stable triangular phase space area, known as the 'stable region' is formed, separating the stable and unstable betatron motion [5]. With a so called 'radio frequency knockout' (RFKO) system, a transverse radio frequency (RF) field, matched to the horizontal tune, is used to stimulate the transverse movement, while the stable region remains constant [12]. For example, if a parti-

cle's revolution frequency is 3.3 MHz and its horizontal tune is 1.680, than we need to use a transverse RF field with a frequency of 5.544 (3.3×1.68) MHz to stimulate the transverse movement. Stored particles are gradually excited with the transverse emittance growth to leave the stable region along the separatrix and extracted by the electrostatic wired septum (ES) and magnetic septa (MS).

The XiPAF synchrotron uses a pair of sextupoles (SR1/SR2) for resonance excitation and another pair of sextupoles (SC1/SC2) for chromaticity correction. SR1 and SR2 are placed symmetrically in the ring. SC1 and SC2 are also placed symmetrically in the ring. The phase advance between SR1 and SR2 is about $5\pi/3$, and they have the same strength but opposite sign, resulting in the same effect on resonance with almost no effect on chromaticity. The phase advance between SC1 and SC2 is also about $5\pi/3$, and they have the same strength and sign, resulting in the same effect on chromaticity with almost no effect on resonance. At XiPAF, the four sextupole magnets are powered by four different power supplies.

The XiPAF slow extraction system is designed without extraction bump orbit and therefore lacks dedicated extraction bump magnets. The ES inner electrode is situated 22 mm from the centre of the tube and can be adjusted by ± 15 mm. In most cases, minor adjustments to the bending magnet (BM) strength or the position of the ES inner electrode are sufficient for the extraction tuning.

Fig. 2 shows the typical beam current and spill intensity signals corresponding to the 10 MeV acceleration and extraction process. The blue curve is the beam current in the ring measured by the DC current transformer (DCCT) and the red curve is the spill intensity measured by the ion chamber (IC) installed in the high-energy beam transport line (HEBT). At 300 ms, the acceleration phase ends and the beam current is ≈ 10 mA corresponding to $\approx 4.4 \times 10^{10}$ protons stored after acceleration. Between 300 ms and 330 ms, the strengths of the sextupole magnets (SR1 and SR2) are ramped up to their design values. In this process, a portion of particles are extracted in advance because their emittance exceeds the area of the stable region. These particles are extracted in a non-RFKO extraction process and are uncontrollable, which are regarded as beam loss. The RFKO system is turned on at 400 ms and ends at 1400 ms, and the RFKO extraction process is indicated by the grey area in Fig. 2.

To facilitate the following explanations, some variables are defined. We define the number of particles reduced in the ring from the start of SR1/SR2 ramping to the end of extraction as N_{total}, corresponding to 300~1400 ms in Fig. 2. We define the number of particles reduced in the ring during the RFKO extraction process as N_{rfko}, corresponding to 400~1400 ms in Fig. 2. Finally, the number of particles extracted to the IC during the RFKO extraction process is defined as n_{rfko}. Based on the variables defined above, in this study we define two types of extraction efficiencies: the total extraction efficiency η_{ex} and the RFKO extraction efficiency $\eta_{ex,rfko}$

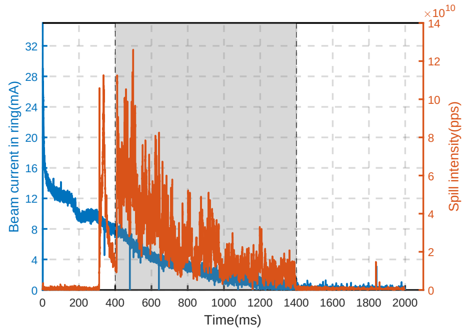

Fig. 2. Typical beam current and spill intensity signals. The blue curve is the beam current in the ring measured by the DCCT and the red curve is the spill intensity measured by the IC installed in the HEBT.

$$\begin{aligned} \eta_{ex} &= \frac{n_{rfko}}{N_{total}} \\ \eta_{ex,rfko} &= \frac{n_{rfko}}{N_{rfko}}. \end{aligned} \tag{7}$$

For the two scenarios discussed in this paper, the common goal is the optimization of efficiency. An increase in total extraction efficiency η_{ex} implies an improvement in RFKO extraction efficiency and a reduction in beam loss for non-RFKO process. Thus, for SEE, the total extraction efficiency can be a suitable optimization target. For MEE, the beam loss during non-RFKO process is represented by another variable called the intensity overshoot ratio. A detailed explanation be can be found in Sec. IV. Intensity overshoot ratio together with the $\eta_{ex,rfko}$ are used for the optimization in MEE.

III. IMPLEMENTATION AT LOW ENERGY SLOW EXTRACTION

A. Low energy extraction at XiAPF

Originally, the XiPAF synchrotron was designed to extract protons in the energy range 60 to 230 MeV. Protons below this energy are typically produced with the addition of an energy degrader. To avoid this, it is planned to extend third-order resonance slow extraction to perform in the range 10~60 MeV.

Space charge effect causes the incoherent and coherent tune shift of the beam and an incoherent tune spread when the beam traverse distribution is not uniform [13]. For 9×10^{10} protons at 10 MeV, the maximum incoherent tune shift $\delta Q_{inc} \approx -0.06$, whilst the tune distance $\Delta Q_{dis} = Q_x - Q_{x,res} = 1.6816 - \frac{5}{3} \approx 0.0149$. A typical tune-diagram with 9×10^{10} protons at 10 MeV with a horizontal bare tune of 1.6816 is shown in Fig. 3. The tune distances of some particles approach zero, and they will

be preliminarily extracted during the SR1/SR2 ramping process. Furthermore, as the extraction progresses, the number of particles decreases and the space charge effect weakens. The tunes of the remaining particles will gradually come back above the $\frac{5}{3}$ resonance line. At this process, some particles would be extracted due to crossing the resonance line rather than by RFKO. These issues finally lead to a low total extraction efficiency with bare tune $Q_x > \frac{5}{3}$. It is therefore proposed that slow extraction be performed with $Q_x < \frac{5}{3}$.

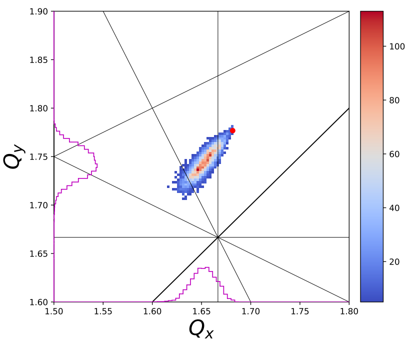

Fig. 3. A typical tune-diagram with 9×10^{10} protons at 10 MeV with a horizontal bare tune of 1.6816.

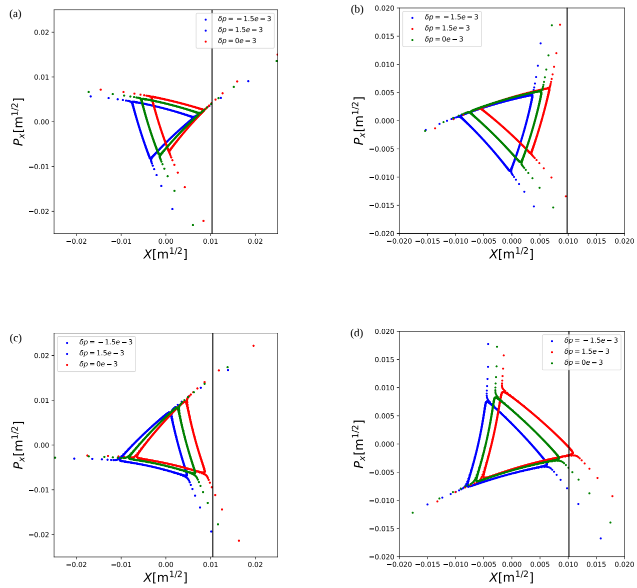

Fig. 4. A schematic of the separatrix distribution flipping in normalized phase space. (a) separatrix distribution at ES entrance with $\Delta Q_{dis} > 0$. (b) separatrix distribution at MS entrance with $\Delta Q_{dis} > 0$. (c) separatrix distribution at ES entrance with $\Delta Q_{dis} < 0$. (d) separatrix distribution at MS entrance with $\Delta Q_{dis} < 0$

However, for the 10 MeV energy extraction with $Q_x < \frac{5}{3}$, the signs of SR1, SR2, SC1 and SC2 have to be changed from $[-,+,-,-]$ to $[+,-,-,+]$ to improve the extraction efficiency [14, 50, 51]. This is because that changing the sign of the tune distance ΔQ_{dis} flips the slow extraction separatrix distribution in phase space. Then, the originally designed 45° angle of the extraction separatrix is no longer optimal, and a suitable angle is assumed to be between 0 and 30°. To illustrate, the schematic of the separatrix distribution flipping in normalized phase space is shown in Fig. 4. As illustrated in Fig. 4(c), after flipping, a particle with a 1.5‰ momentum deviation first enters ES with $P_x < 0$ and will be lost in ES. Furthermore, as illustrated in Fig. 4(d), after flipping, particles are susceptible to be lost at MS due to the aperture constraints. They are lost before entering ES, which reduces the extraction efficiency. The above phenomenons don't occur when the tune distance $\Delta Q_{dis} > 0$.

Modifying the positions of the sextupole magnets on the ring can alter the angle, but this is evidently more laborious and less convenient for extraction tuning. At XiPAF, the four sextupole magnets have different power supplies. Therefore, we choose to change the signs and optimize the strengths. Thus, the roles of SR and SC are no longer independent and more time was spent on scanning the four sextupole strengths. This is the main reason for the increase of beam commissioning time. Apart from the sextupole strengths, the operators have to adjust other parameters such as the tune, the closed orbit at the entrance of the ES, the strengths of the ES and MS and so on.

Therefore, the beam extraction tuning at the 10 MeV energy took several days, while one day is sufficient for the normal commission of the extraction of a new energy above 60 MeV. The total extraction efficiency at 10 MeV was optimized to exceed 65% with $4.5 \sim 6.5 \times 10^{10}$ protons stored before extraction by setting the horizontal tune below the third-order resonance (5/3) and using a high multiple-frequency RFKO signal [14, 50].

What's more, under low energy extraction conditions, due to the influence of the space charge effect, the optimal parameters tend to be strongly correlated with the beam intensity before extraction. Consequently, if there is a significant change in the beam intensity on any given day, the optimal parameters shift accordingly, requiring additional time for fine tuning the extraction.

We selected seven tuning parameters for the BO based on their influence on the extraction process and the prior knowledge of experienced operators. The parameters are the strengths of 4 sextupole magnets, the focusing quadrupole (QF) magnet strength, the defocusing quadrupole (QD) magnet strength and the BM strength. The strengths of 4 sextupole magnets determine the size of the stable region, the spiral step and the angle of the separatrix in phase space. The strengths of the QF and QD magnets mainly determine the horizontal tune which subsequently affects the size of the stable region and the spiral step. In this section, the optimization goal for SEE is to maximize the total extraction efficiency η_{ex}.

B. Optimization results in simulation

Before deploying the algorithm in the accelerator, BO is first tested by simulation. The primary objective of the simulation is to verify the feasibility of BO applied to the extraction tuning below the resonance, i.e., to obtain an extraction efficiency comparable to manual optimization result within a limited number of evaluations. In the simulation, a manually optimized value of 81% for the total extraction efficiency was obtained for the case of extraction below the resonance[51]. A secondary objective is to compare BO with other algorithms.

The extraction process is simulated by Syntrack [50], which was developed based on Li-track [52] with more functions and better usability. The simulation consists of 35,000 turns, with the first 5,000 turns corresponding to the sextupole magnet ramping up, and the subsequent 30,000 turns corresponding to the RFKO extraction process. The number of macro-particles in the simulation is 10000. Based on the particle loss positions at the ring and the number of turns, the values of n_{rfko}, N_{total} and η_{ex} can be obtained from the simulation. Space charge force is not considered in the simulation due to time constraints. Therefore, the influence of tune spread and shift caused by space charge force won't be reflected in the simulation. The optimal parameters setting in the simulation will also differ from the experiment.

The BO algorithm is tested using seven tuning parameters as illustrated in Sec. III A. Seven parameters have been set with specific bounds. Within these limits, the range of variation for the horizontal tune is from 1.6590 to 1.6648. The average closed orbit shift caused by changes in bending magnet strength ranges from -1.3 to 1.3 mm. The strength range for each of the sextupole magnets is from 0 to 12.5 m^{-3}. Within the simulation, the boundaries are MIN-MAX normalized in the algorithm.

Before showing the results of BO, we first give the results of 500 evaluations with the random uniform sampling method, as shown in Fig 5. As illustrated Fig 5, only 7 evaluations have a total efficiency greater than 85%. Therefore, it can be known that finding a parameters setting with high extraction efficiency within the ranges listed above is not a high probability event with parameters sampled randomly.

In the simulation with BO, the UCB and EI acquisition functions are used and the parameter κ for UCB is set to 2.5 and ξ for EI is set to 0.01. The results of the seven-dimensional problem using two different acquisition functions are shown in Fig. 6.

Fig. 6 shows the optimization results over 10 optimization runs using UCB and EI acquisition functions. Each run starts from a detuned setting. The settings and the random seeds among ten runs are different. The total extraction efficiencies at the detuned settings are less than 10%.

It is observed that the average efficiency demonstrates a not increasing trend following approximately 20∼30 evaluations. For each optimization run in Fig. 6, a parameters setting with a total extraction efficiency greater than 85% can be found within 32 evaluations. The maximum total efficiency in all 20 runs within 80 evaluations is 89.7%.

In addition, the results of multiple runs show significant fluctuations, which may be due to the large parameter space in a seven-dimensional problem, where the algorithm tends to explore more. When a better point

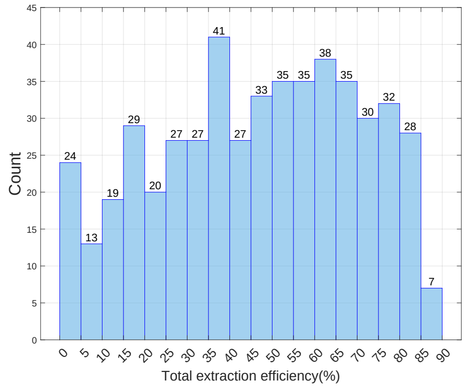

Fig. 5. Results of 500 evaluations with the random uniform sampling method

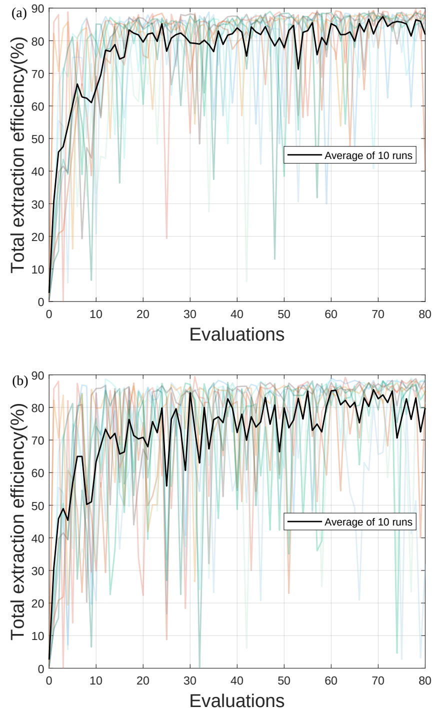

Fig. 6. Optimization results of the total extraction efficiency using EI and UCB acquisition functions for the seven-dimensional problem. (a) shows the results with EI and (b) shows the results with UCB. The black line is the average total extraction efficiency over ten runs. The lines with other colours depict the results of ten runs with different detuned settings.

is probed, the algorithm does not 'exploit', but continues to explore the next perceived better point. When the next point is not optimal, there is a sudden drop in extraction efficiency, so the whole process exhibits oscillatory results. The fluctuation of results can be reduced by introducing safety constraints.

For comparison, we have conducted the same optimization process using the Nelder-Mead algorithm (NM) [21], which is a widely used numerical optimization technique in the accelerator community and considered as a standard benchmark [23]. This method meticulously monitors $d+1$ (d refers to the dimension of the parameter space) evaluation points and constructs a simplex based on these data points. The Nelder-Mead algorithm efficiently finds the optimal solution via geometric modifications of the stored simplex, and has been proven to converge at a relatively rapid rate. The results of this algorithm are shown in Fig. 7.

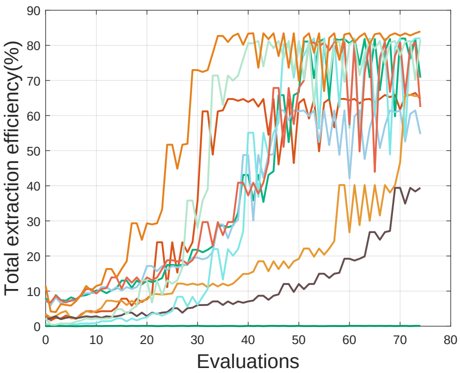

Fig. 7. Optimization results using NM for the seven-dimensional problem. The lines depict the results of ten runs with different colours.

In Fig. 7, each run starts from a detuned setting and the settings among ten runs are different. The 10 detuned settings are same with the runs used in Fig. 6 for comparison. The convergence rate of the Nelder-Mead algorithm depends significantly on the choice of initial step parameters. In terms of convergence rate, the fastest case requires about 30 evaluations, and in some cases there is no obvious convergence trend after 75 evaluations. From the convergence results, the extraction efficiency can be optimized to 84%. However, in certain cases they end up at local optima with extraction efficiency no greater than 70%, and in some cases, even less. Therefore, in order to prevent Nelder-Mead from breaking down and force exploration of the parameter space, it is usually designed to be automatically restarted when the step becomes too small.

From the above results and discussion, it can be concluded that BO is more effective than NM for the seven-dimensional problem, as it achieves a high-efficiency parameters setting with a faster rate.

In a particular run with the UCB acquisition function, the extraction efficiency reached 89% after 31 evaluations. We select the seven parameters corresponding to this evaluation to show the associated extraction parameters. We present the extraction arms corresponding to different momentum deviations in the normalized phase space, the beam phase space plot at ES, and the envelope changes during the last three turns before entering ES, as shown in Fig. 8.

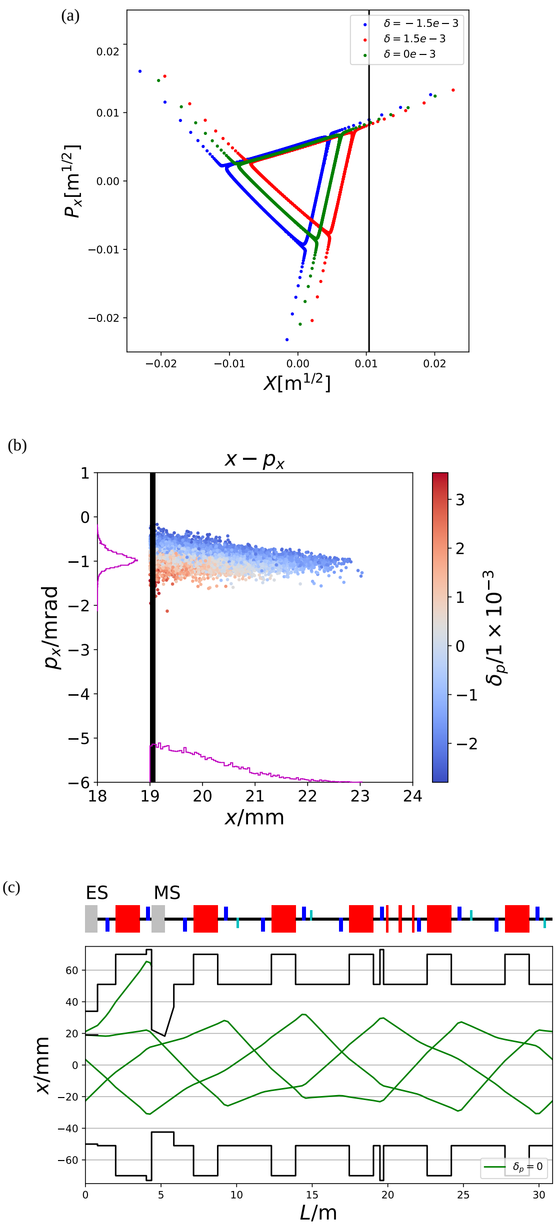

Fig. 8. With an optimal parameters setting, (a) is the schematic diagram of the extraction arms corresponding to different momentum deviations in the normalized phase space, (b) is the phase space plot at ES, and (c) shows the envelope changes during the last three turns before entering ES.

In Fig. 8(a), the extraction arms for particles with momentum deviations of $\pm1.5‰$ and 0 are shown in the normalized phase space, which basically coincide. The

difference between the P_x at the ES inner electrode for particles with momentum deviation of $-1.5‰$ and $1.5‰$ is only about $0.5 \times 10^{-3}\mathrm{m}^{\frac{1}{2}}$, which translates to a radian of 0.41mrad. This means a small beam angular spread at ES and the extraction efficiency improved.

Fig. 8(b) is the phase space plot at ES and shows a multi-particles simulation result obtained using Syntrack. The angular spread and spiral step information at ES can be observed. At x =19 mm, the angular spread is about 1 mrad and the spiral step is about 2 mm. In the simulation, the tilt angle of ES is set to -1.25 mrad. Consequently, the mean value of p_x is optimized to approach -1.25 mrad, thereby minimizing the probability of particle loss in ES.

Fig. 8(c) shows the envelope changes during the last three turns for particles with zero momentum deviation. When the momentum deviation is small, the envelope does not exceed the aperture limit within the ring, indicating that the beam loss is primarily due to the larger momentum dispersion at lower energies.

C. Experimental optimization results

In this section, we describe the results of the BO algorithm implemented at the XiPAF synchrotron low energy extraction tuning. Due to the lack of noise and space-charge effects in the simulation, the main objective of the experiment is to perform the BO algorithm to optimize extraction on the actual machine to confirm the simulation results.

Due to time constraints, the program was not implemented within the accelerator control system. Therefore, in the experiment, all seven parameters were manually adjusted in the control system and the extraction efficiency was also manually updated to the algorithm. The parameters manually adjusted will increase the time and cost of one evaluation. It is important to note that this does not detract from the significance of applying BO. The advantage of BO is that it reduces the number of evaluations compared to other algorithms. It is therefore reasonable to expect the application of BO with parameters automatically adjusted and updated in the future. This will greatly speed up the tuning procedure.

In the experiment, the change in magnetic field strength is achieved by adjusting the gain (g) of the magnet current curve. The manually optimized current curve gains g_{SR1}, g_{SR2}, g_{SC1}, g_{SC2}, g_{BM}, g_{QF} and g_{QD} are shown in Tab. 1. As the requirement for extraction with $Q_x < \frac{5}{3}$ was not considered in the initial design phase of the power supply, the SC power supplies are insufficient to provide the current required. Therefore, the values of g_{SC1} and g_{SC2} are set to 1 in Tab. 1.

With the parameters in Tab. 1, the average closed orbit of 6 beam position monitors (BPM) is about -0.4 mm, the horizontal bare tune is about 1.6606 and the total extraction efficiency defined above is 58.9%. With the same parameters setting, the total extraction efficiency has reached more than 65% by Y. Yang. 58.9% is less than 65%, indicating that the optimal parameters have drifted.

TABLE 1. Manually optimized current curve gains

Gain	Value	Gain	Value
g_{SR1}	0.1	g_{SR2}	0.1
g_{SC1}	1	g_{SC2}	1
g_{QF}	0.904	g_{QD}	0.9
g_{BM}	0.9		

In this experiment we have set the optimization bounds for the current curve gains. For SR and SC, the current curve gain bounds are set to [0, 1]; for BM, the gain bound is set to [0.8964, 0.9036], with the upper and lower bounds values corresponding to approximately $\pm$ 1.2 mm closed orbit variations; for QD, the gain bound is set to [0.891, 0.909]; for QF, the gain bound is set to [0.895, 0.913]. The current curve gain adjustment ranges for QF and QD correspond to approximately $\pm$ 0.006 horizontal bare tune adjustment ranges. Within the experiment, the boundaries are not MIN-MAX normalized in the algorithm.

The UCB and EI acquisition functions are used and the parameter κ for UCB is set to 2.5 and ξ for EI is set to 0.01. The optimization run with BO was performed for a fixed number of evaluation steps: 50 steps. This corresponds to about 2~3 hours for each optimization run, where most of the time was spent on manually setting the parameter values and evaluating the extraction efficiency. The computation time of the GP model and the acquisition function is negligible, and due to the machine time constraints, only two runs with UCB and EI acquisition functions were tested. So, this experiment is more of a proof-of-principle experiment: to verify that BO based on Gaussian process modelling is feasible for the black-box function optimization problem of slow extraction efficiency below the resonance with strong space charge effect.

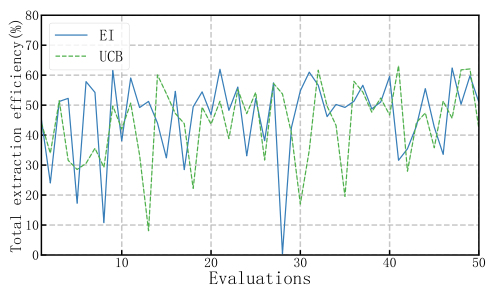

Fig. 9. Experimental optimization results of the total extraction efficiency using BO with two different acquisition function. UCB (green, dashed) and EI (blue, solid) have similar results and are both able to optimize the extraction efficiency within a reasonable number of evaluations.

Fig. 9 shows the results of the experimental optimiza-

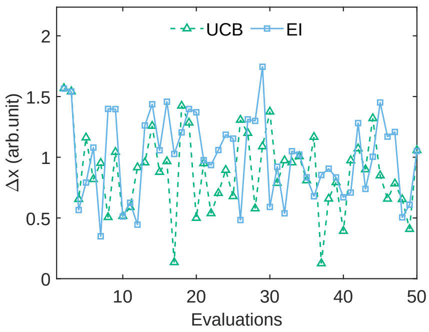

Fig. 10. Behaviour of BO with UCB (green, dashed, triangle) and EI (blue, solid, square) acquisition functions on the seven-dimensional problem. The distance Δx between two successive sampled points is shown in the Min-Max scaled parameter space.

tion. The parameters of the first step are randomly assigned and the same random seed is used for the UCB and EI evaluations. Both EI and UCB acquisition functions are able to find a parameters setting with $\eta_{ex} > 60\%$ within 50 evaluation steps.

We have also observed and made preliminary analyses of some other phenomena. Firstly, there is no clear upward trend in the early evaluations, which may be due to the relatively high extraction efficiency of the first step and the fast optimization speed. Secondly, the performance of both UCB and EI also presents oscillatory, non-convergent results, which could be attributed to more exploration in the large parameter space. This phenomenon also appears in the simulation with a large parameter space.

The distances Δx between two successive sampled points of BO for the seven-dimensional problem is shown in Fig. 10. It can be seen that BO with UCB and EI acquisition functions show significant fluctuations, reflecting that BO generally samples at a larger distance and does not become trapped in local optima. The evolution of seven current curve gains during the evaluations is shown in Fig. 11. It can also be seen that the current curve gains fluctuate during optimization, especially for g_{BM}, g_{QF} and g_{QD}.

In this experiment, we validated the feasibility of applying BO to the slow extraction efficiency optimization. For the relatively extreme scenario of low-energy slow extraction, BO is also applicable.

IV. IMPLEMENTATION FOR MULTIPLE-ENERGY EXTRACTION

The schematic diagram of MEE is shown in Fig. 12(a). The ability to deliver several energy steps per accelerator cycle reduces the time spent on the reaccelerating the beam during patient treatment and improves the treatment efficiency [53].

In MEE, after the extraction of the initial energy step,

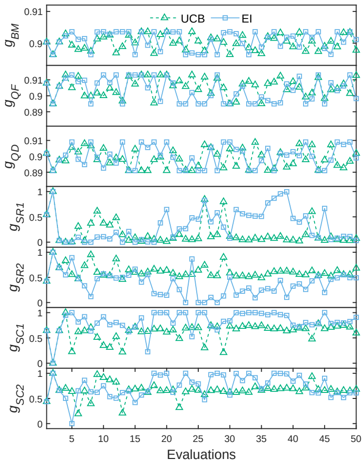

Fig. 11. The evolution of the input parameters is shown over the evaluations including two runs using BO with UCB (green, dashed, triangle) and EI (blue, solid, square) acquisition functions.

the synchrotron decelerates remaining particles to the next lower energy step. An intensity overshoot causing uncontrollable spilled beams will be induced by the emittance growth due to the deceleration. Fig. 12(b) illustrates the process of overshoot formation with the radial distribution function of particles in normalized phase-space (X, X'). The blue solid line represents the radial distribution at time t_0, which corresponds to the end of the E_1 energy step as shown in Fig. 12(a). The blue dashed line represents the radial distribution at time t_1, which corresponds to the start of the E_2 energy step as shown in Fig. 12(b). r_1 and r_2 represent the boundary of the stable region for E_1 and E_2 respectively.

From t_0 to t_1, the beam is decelerated and the transverse emittance increases, causing the radial distribution of the beam to change from the blue solid line to the dashed line. To illustrate, let us consider the horizontal geometric RMS emittance at t_0 and t_1 to be $\varepsilon_{x,1}$ and $\varepsilon_{x,2}$ respectively. It is assumed that the normalized emittance remains constant during the deceleration, therefore, it can be concluded that $\varepsilon_{x,2} = \varepsilon_{x,1}\frac{p_1}{p_2}$, where p_1 and p_2 represent the corresponding momentum of E_1 and E_2. Deceleration means $p_2 < p_1$, so $\varepsilon_{x,2} > \varepsilon_{x,1}$. Therefore, during the sextupole magnets ramping up at the E_2 energy step, particles whose $r > r_2$ are prematurely extracted, forming a spill intensity overshoot. The number of particles reduced during this process is defined as N_{os}.

It is essential to prevent this overshoot, as a significant overshoot in beam intensity can lead to the formation of a dose hot-spot within the target volume [17]. Therefore, a fast beam chopper system has been installed in the high-energy beam transport line (HEBT) at HIMAC to prevent uncontrollable spilled beams from being delivered to the irradiation port [17]. The overshoot and other uncontrollable beam are removed and blocked in the beam dump by the chopper system, more impor-

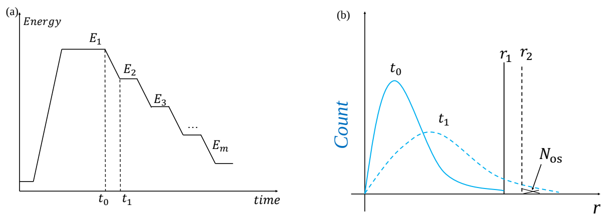

Fig. 12. Schematic diagrams used to illustrate the processes related with MEE. (a) shows the energy variation within a single accelerator cycle. (b) shows the transverse radial distribution variation before and after the deceleration and it also illustrates the process of intensity overshoot formation.

tantly, such beam loss should be reduced.

The spill intensity overshoot can be reduced by adjusting the size of the stable region area. From Fig. 12, it is evident that the larger r_2/r_1 is, the fewer the number of overshoot particles N_{os}. In this method, each energy step E_i has its corresponding stable region area A_i, and it is designed such that

$$\frac{A_i}{A_{i-1}} = P_i > 1, (i \geq 2). \tag{8}$$

This method has been used by HIMAC to reduce the intensity overshoot and P_i or A_i is pre designed as a fixed value [18]. With this method, a high overall efficiency across all energy steps can be achieved.

It is anticipated that the application of BO to MEE will facilitate and speed up the extraction tuning process. In this section, we demonstrate through simulations that it is possible to improve the RFKO extraction efficiency while controlling the stable region area within a limited number of evaluations. Although experimental conditions are not currently available at XiPAF, our validation work will provide other organizations with a reference for the selection of relevant algorithms when tuning MEE.

A. Optimization parameters and the objective function

One of the main factors affecting the extraction efficiency is the spiral step. The equation of spiral step ΔR is shown as follow

$$\begin{aligned}\Delta R = \epsilon X_1' + \frac{3}{4} S\{\sin(3\Delta\mu)(X_1^2 - X_1'^2) \\ + 2\cos(3\Delta\mu) X_1 X_1'\}.\end{aligned} \tag{9}$$

where $\epsilon = 6\pi(Q_x - Q_{x,res})$, S is the normalized strength of the virtual resonance excitation sextupole, $\Delta\mu$ is the phase advance from the resonance excitation sextupole to the ES and $(X_1, X_1') = (X_{ES} - X_{co}, X_{ES}' - X_{co}')$. (X_{ES}, X_{ES}') is the intersection coordinate of separatrix and the ES inner electrode coordinate in the normalized phase space. (X_{co}, X_{co}') is the coordinate of the closed orbit at ES entrance in the normalized phase space.

From Eq. (9), the spiral step depends mainly on the extraction bump orbit, the horizontal tune and the resonance sextupole strength. The area of the stable region is determined by the horizontal tune and the resonance sextupole strength. Therefore, when there is a extra need for enhanced control of the stable region area, the position of the extraction bump orbit and its angle can be considered as new parameters to be optimized in order to achieve superior optimization outcomes.

In this section, the optimization is also carried out based on XiPAF. XiPAF is not equipped with a group of extraction bump magnets. Therefore, the extraction bump orbit is formed by the horizontal closed-orbit correction magnets. So except for QF, QD, SR, SC strength, the extraction bump orbit position x_{co} and the angle x_{co}' at ES are two new parameters to be optimized in this section.

The following is a brief explanation of how to determine the strengths of the horizontal correction magnets required for the extraction bump orbit at ES. The positions of the six horizontal correction magnets: HC02, HC04, HC06, HC08, HC10 and HC12 can be seen in Fig. 1. There are also six beam position monitors (BPM02∼12) installed at the ring, which are located at the same positions as the corresponding horizontal correction magnets. To uniquely determine the strengths of HC02∼12 , six independent constraints are needed. With the constraints on the orbit position and angle at ES already in place, four additional constraints are required. Closed orbits at BPM02, 08, 10, and 12 are set to zero as the remaining four constraints. As for an example, where the $x_{co} = 6\ mm$ and $x_{co}' = 0\ mrad$, a set of HC02∼12 strengths required can be matched, and the corresponding ring's closed orbit is shown in Fig. 13.

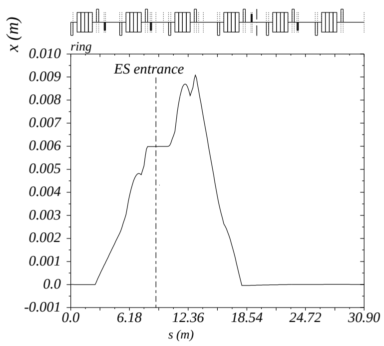

Fig. 13. Schematic diagram of the ring's overall closed orbit variation. The closed orbit position and angle at ES is 6 mm and 0 mrad.

N_{os} reflects the absolute size of the intensity overshoot. However, our interest also extends to the relative size of the intensity overshoot. Therefore, we define a variable called the intensity overshoot ratio η_{os} to facil-

itate the subsequent discussion. It is defined as

$$\eta_{os} = \frac{N_{os}}{N_{rm}}, \tag{10}$$

where N_{rm} refers to the number of particles that remain in the ring prior to the implementation of sextupole ramping.

Now we turn to the design of the objective function. Unlike the optimization objective in the Sec. III, this section deals with a multi-objective optimization problem. Besides aiming for a high RFKO extraction efficiency, we also want the area of the stable region to be as close as possible to a target value. Considering that the area of the stable region is not an easliy measurable physical quantity, we choose to use the overshoot ratio η_{os} as a proxy for the area of the stable region. From Fig. 12(b), it is known that as long as the beam distribution remains unchanged before the sextupole magnets ramping up, η_{os} and the stable region area can be considered as a one-to-one correspondence. From another point of view, the demand for area control in practical applications is essentially a demand for controlling the overshoot ratio. And it is practical to use the overshoot ratio as an optimization objective without spending extra time to measure the horizontal tune to compute the area of the stable region.

Given the definitions and explanations above, the optimization objectives are clear: $\eta_{ex,rfko}$ should be as high as possible, and η_{os} should be as close as possible to the target overshoot ratio $\eta_{os,t}$, i.e.,

$$\begin{aligned} &max\ \eta_{ex,rfko}, \\ &min\ |\eta_{os} - \eta_{os,t}|. \end{aligned} \tag{11}$$

For such a multi-objective optimization problem, we attempt to condense the two objectives into a single figure of merit, thus converting it into a single-objective optimization problem. Though in multi-objective optimization, the true goal is to find the Pareto front (PF). For the sake of convenience, we choose the aforementioned approach since we consider that the two objectives do not exhibit strong competition by introducing the extraction bump orbit position and angle as parameters to be optimized.

We propose the following form of the objective function

$$f(\eta_{ex,rfko}, \eta_{os}) = \begin{cases} \eta_{ex,rfko} e^{-\frac{|\eta_{os}-\eta_{os,t}|}{\omega}}, \ e^{-\frac{|\eta_{os}-\eta_{os,t}|}{\omega}} > k \\ \eta_{ex,rfko} k, \ e^{-\frac{|\eta_{os}-\eta_{os,t}|}{\omega}} \leq k \end{cases}, \tag{12}$$

where k and ω are hyper-parameters that need to be set based on the specific situation. The exponential term reflects the penalty effect on the RFKO extraction efficiency. The hyper-parameter ω determines the rate of decay of the exponential term. The piecewise design is considered because, during the actual optimization, there have been instances where a large overshoot ratio causes the exponential decay term to approach zero, making the figure of merit insensitive to variations in RFKO extraction efficiency. So, when the exponential term is smaller than k, the RFKO extraction efficiency is only penalized by a fixed value of k.

B. Optimization results in simulation

In this section, we will verify the feasibility of applying BO to such a multi-objective extraction process through simulation. Since XiPAF currently lacks the experimental conditions, we artificially introduce a certain amount of output noise, to demonstrate the efficacy of BO with observation noise. For the hadron therapy, the required proton energy range is approximately 60∼230 MeV. Furthermore, the influence of the space charge effect on slow extraction can be disregarded. Consequently, the conditions and process of the simulation are similar to those described in Sec. III B, with the exception that the extraction simulation is conducted with $Q_x > \frac{5}{3}$ and a proton energy of 60 MeV.

As an example, consider the beam tuning for an energy step in MEE. It is assumed that the designed stable region area A_0 for this step is 21.7 $\pi\ mm \cdot mrad$. In the event of an unoptimal parameters setting with a horizontal tune of 1.6800 and an area of A_0 with no extraction bump orbit at ES, the RFKO extraction efficiency is 86% and the overshoot ratio is 6.88% in the simulation. We aim to find a set of better extraction parameters that maximize the RFKO extraction efficiency while keeping the stable region area or the overshoot ratio of 6.88% unchanged.

After determining the specific optimization objectives, we first identify the specific parameters to be optimized and their ranges. For the extraction above the third-order resonance, the strengths of SR1 and SR2 are identical and their signs are fixed as [-,+]. The strengths of SC1 and SC2 are also identical but their signs are fixed as [-,-]. Therefore, only two absolute strength values of the SR and SC are selected as the optimization parameters. Including the QF strength, QD strength, ES closed-orbit position and angle, there are a total of six parameters to be optimized in the simulation. Each of these six parameters has a defined bound. Within the bounds,

the horizontal tune can vary between 1.6741 and 1.6817, the stable region area can vary approximately between 6.5∼32.1 $\pi mm \cdot mrad$, and the horizontal chromaticity can vary between -0.21 and -0.76. The closed-orbit position at ES entrance x_{co} ranges from 0 to 6 mm, and the closed-orbit angle x'_{co} ranges from -1.5 to 1.5 mrad. Within the simulation, the boundaries are MIN-MAX normalized in the algorithm.

Having determined the specific parameters to be optimized, we now discuss the determination of the hyperparameters in Eq. 12. We know that $\eta_{os,t}$ is 6.88%. We preliminarily choose $\omega = 0.13$, which is approximately twice $\eta_{os,t}$. Additionally, k is preliminarily taken as 0.2, corresponding to a breakpoint $\eta_{os} = 0.28$. An overshoot ratio of 28% is already quite large, so we do not consider the penalization effect of even larger η_{os}, preventing the exponential term from approaching zero under large η_{os}. Then, a specific objective function is shown as follow.

$$f(\eta_{ex,rfko}, \eta_{os}) = \begin{cases} \eta_{ex,rfko} e^{-\frac{|\eta_{os}-0.0688|}{0.13}}, & e^{-\frac{|\eta_{os}-0.0688|}{0.13}} > 0.2 \\ 0.2\eta_{ex,rfko}, & e^{-\frac{|\eta_{os}-0.0688|}{0.13}} \leq 0.2 \end{cases} \tag{13}$$

Next, we discuss the impact of noise. Between the two parameters: RFKO extraction efficiency and overshoot ratio, the fluctuation in RFKO extraction efficiency is often small, on the order of 1%, while the fluctuation in the overshoot ratio is typically larger. The main reason for the larger fluctuation in the overshoot ratio is the poor reproducibility of the beam distribution over different machine cycles. Based on historical data, the standard deviation of the overshoot ratio fluctuation can reach up to 10%. Therefore, to take into account the effect of the overshoot ratio fluctuation, the η_{os} is calculated using the formula below

$$\eta_{os} = \eta_{os,ori} + \eta_{err}, \eta_{err} \sim N(0, 0.1\eta_{os,t}), \tag{14}$$

where $\eta_{os,ori}$ refers to the original overshoot ratio, as obtained from the Syntrack simulation and η_{err} is a normally distributed random variable with mean zero and standard deviation of 0.1 times $\eta_{os,t}$. With considering the impact of noise, the σ_{noise} parameter in the Gaussian process has also been appropriately adjusted.

In this optimization process, the UCB and EI acquisition functions are used, with the parameter κ for UCB set to 2.5 and ξ for EI set to 0.01. The optimization results are shown in Fig. 14.

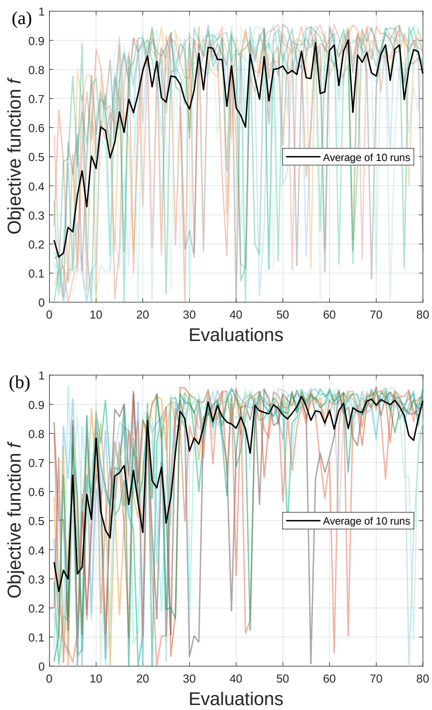

Fig. 14. Optimization results using EI and UCB acquisition functions for the six-dimensional problem. (a) shows the results with EI and (b) shows the results with UCB. The black line is the average result over ten runs. The lines with other colours depict the results of ten runs with random initial settings.

As illustrated in Fig. 14, the average objective function over ten runs demonstrates a not increasing trend following approximately 20∼30 evaluations. For each optimization run in Fig. 14, a parameters setting with the objective function greater than 0.9 can be found within 35 evaluations, and grearter than 0.94 within 50 evaluations. The maximum total efficiency in all runs is 0.96.

To gain a more intuitive understanding of the optimization outcomes for RFKO extraction efficiency and overshoot ratio, the variations in RFKO extraction efficiency and overshoot ratio with the number of evaluations during a specific run are presented in Fig. 15.

As illustrated in Fig. 15, the extraction efficiency in this run exhibited a potential for optimization exceeding 95%, with an overshoot ratio approximating 0.0688. Based on these observations, it can be postulated that the anticipated optimization objectives have been met through the application of BO and the designed objective function.

In the optimization runs corresponding to Fig. 15, the variations in the ratio g of QF, QD, SR, and SC strengths, as well as the variation of x_{co} and x'_{co} are shown in Fig. 16.

Taking the parameters from the 48th evaluation in the above EI run as an example. For this evaluation, the horizontal tune is 1.680, RFKO extrac-

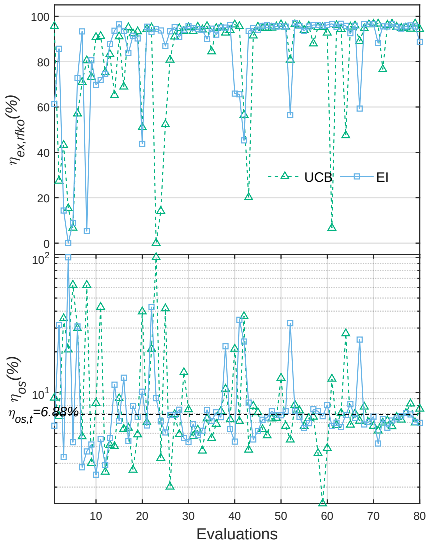

Fig. 15. Variations of RFKO extraction efficiency and overshoot ratio using UCB (green, dashed) and EI (blue, solid) acquisition functions for the six-dimensional problem during a specific run.

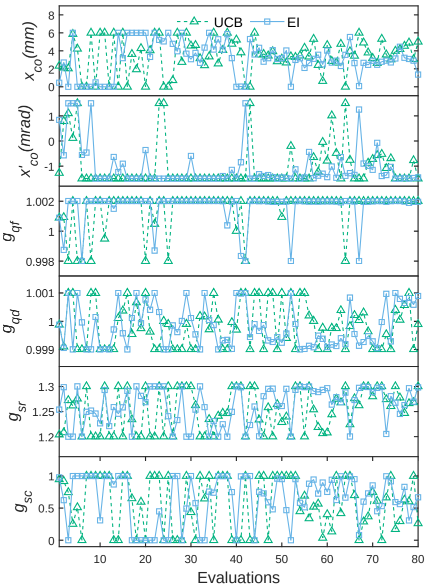

Fig. 16. The evolution of the input parameters is illustrated over the evaluations including two acquisition functions: UCB (green, dashed, triangle) and EI (blue, solid, square).

tion efficiency is 95.8% and the stable region area is 21.6 π mm $\cdot$ mrad, which closely aligns with the target area value 21.7 π mm $\cdot$ mrad. The ES closed orbit position and angle are 4.1 mm and -1.4 mrad. The corresponding ring's overall closed orbit variation is shown in Fig. 17.

In conclusion, the simulation results presented above provide evidence that the application of BO to MEE is a viable approach. Despite the absence of experiments, the

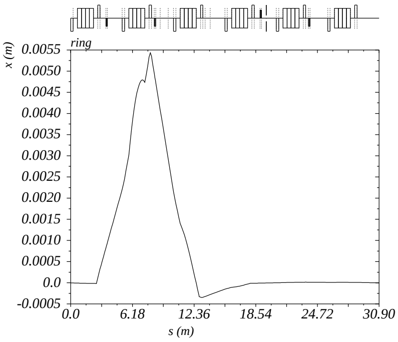

Fig. 17. Schematic diagram of the ring's overall closed orbit variation. The closed orbit position and angle at ES is 4.1 mm and -1.4 mrad.

optimization of parameters at the design stage through simulation is also meaningful, as it provides a reference for actual beam tuning.

V. DISCUSSION

We have mentioned that the intensity overshoot is caused by emittance growth due to the deceleration. This can be avoided by re-accelerating from low to high energy, but there are some problems with this option. In hadron therapy, a tumor is typically irradiated from a deep slice to a shallow slice, which means that the required beam energy should change from high to low energy. In addition, due to the space charge effect, the synchrotron can store more particles at high beam energy. For example, the number of particles that XiPAF synchrotron can store at 200 MeV is about twice as many as at 60 MeV. To store more particles, and considering the tradition of hadron therapy, MEE from high to low energy is chosen as the basis for our study.

The relationship between the intensity overshoot ratio η_{os} and the stable region area A in simulation is shown in Fig. 18. The horizontal RMS emittance in the simulation is 3 π mm $\cdot$ mrad. The relationship between η_{os} and A is not linear, as shown in the Fig. 18. As A decreases, the growth rate of η_{os} increases. This is due to the fact that the tranverse radial distribution resembles the Rayleigh distribution, as shown in Fig. 12(b). Therefore, in the actual optimization stage, we need to make η_{os} larger, so that η_{os} is more sensitive to the variation of the stable rgion area. The η_{os} caused by the deceleration is around 1% or even less in the experiment. Therefore, in the optimization stage of an energy step, the emittance needs to be intentionally increased before the SR ramping. This can be achieved by pre-excitation with RFKO. It is important to note that this extra pre-excitation process is not required in the actual treatment stage.

In MEE simulation, random noise is introduced to the intensity overshoot. It is acknowledged that a more real-

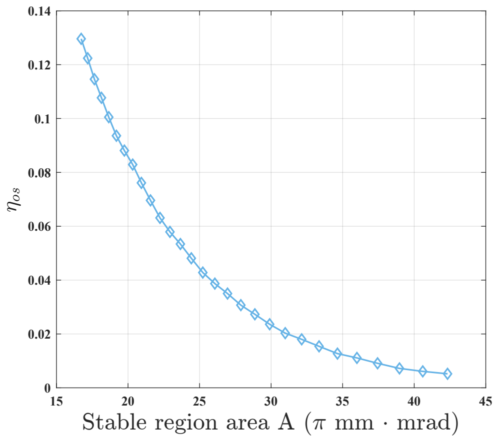

Fig. 18. Schematic of the relationship between the intensity overshoot ratio η_{os} and the stable region area A in simulation. The horizontal RMS emittance in the simulation is 3 π mm $\cdot$ mrad.

istic approach would be to add noise equivalent to conditions seen in the accelerator, and their causes, e.g. power converters. However, adding the noise of the actual situation involves the specific spectrum and amplitude of the ripple, the beam distribution jitter, and other factors. The straightforward approach of introducing noise to the output is a simple method that is employed in simulation to verify the reliability of BO in the context of output nosie. In the event of a suitable opportunity arising, experimental validation of the BO applied to MEE is scheduled to take place.

Finally, a concise discussion is provided herein on the implementation of BO to the accelerator control system. The process variables of the control system currently contain the magnets' DC values, the outputs of measurement devices such as the DCCT, BPM and IC, and so on. So some simple beam tuning tasks are currently automated at XiPAF. For example, the parameters grid scanning is applied for the optimization of low-energy beam transport line (LEBT) and the synchrotron injection process. But current curve gains, extraction efficiency and the extraction overshoot ratio are not process variables yet. One reason for this is that the power supply design does not take into account the control of the current curve gains, which can only be set manually. Another reason is that the extraction efficiency and the overshoot ratio currently rely on manually reading the DCCT and IC results and using additional scripts for the calculations. So in order to automate the operation of BO, the above two problems need to be solved. On the one hand it is desired that the current curve gain can be automatically controlled as a process variable. Or just set a target value of the current flattop and the power supply can automatically generate transition curves between different flattops. On the other hand, it is desired to integrate the processing scripts for the extraction efficiency and overshoot ratio into the control system. Finally, with the the BO algorithm relized in the control system program, the automatization of BO can be expected.

VI. SUMMARY

This article presents the application of Bayesian optimization to the third-order resonance slow extraction process. The focus is on two scenarios of slow extraction, with the XiPAF synchrotron serving as a testbed.

Firstly, the optimization of total extraction efficiency for SEE below the third-order resonance was described, and the algorithms were tested in simulation and a proof-of-principle experiment. Due to time constraints, only two runs were tested in the experiment. For the extraction below the resonance, the strengths of the four sextupole magnets need to be individually optimized, which increases the beam tuning time. Our findings demonstrate that BO is an effective method for optimizing the total extraction efficiency for SEE in a limited number of evaluations. Additionally, we have shown that BO outperforms the commonly used Nelder-Mead method in simulation.

Secondly, we demonstrated the application of the BO method to maximize the RFKO extraction efficiency while controlling the stable region area in MEE. In order to address this multi-objective optimization problem, the intensity overshoot was employed as a proxy for the area of the stable region, and the extraction bump orbit position and angle were included as optimization parameters. In light of the distinctive nature of the intensity overshoot, we delineate the design of the objective function, which condenses the two objectives into a single figure of merit. To substantiate the efficacy of our approach, we conducted a simulation wherein random noise is introduced to the intensity overshoot. The results demonstrate that BO can rapidly optimize the objective function while yielding the anticipated outcomes. As demonstrated in the example, the RFKO extraction efficiency can be enhanced to above 95% and the intensity overshoot ratio closely aligns with the target area value 0.0688.

VII. BIBLIOGRAPHY

[1] V. Kain, F. M. Velotti, M. A. Fraser et al., Resonant slow extraction with constant optics for improved separatrix control at the extraction septum. Phys. Rev. Accel. Beams 22, 101001 (2019). doi: 10.1103/PhysRevAccel-

Beams.22.101001

[2] S. Ruan, J. Yang, J. Zhang et al., Design of extraction system in bring at hiaf. NUCL. INSTRUM. METH. A 892, 53–58 (2018). doi: /10.1016/j.nima.2018.02.052

[3] P. Spiller, G. Franchetti, The FAIR accelerator project at GSI. NUCL. INSTRUM. METH. A 561, 305-309 (2006). doi: 10.1016/j.nima.2006.01.043

[4] K. Sato, S. Yamada, H. Ogawa et al., Performance of himac. Nucl. Phys. A 588, c229-c234 (1995). doi: 10.1016/0375-9474(95)00144-P

[5] L. Badano, M. Crescenti, P. Holy et al., Proton-Ion Medical Machine Study (PIMMS), 1. Technical report, 1999. No. CERN PS-99-010-DI. doi: 10.1093/comjnl/7.4.308

[6] J. Shi, J.C. Yang, J.W. Xia et al., Heavy ion medical machine (HIMM) slow extraction commissioning. NUCL. INSTRUM. METH. A 918, 76-81 (2019). doi: 10.1016/j.nima.2018.11.014

[7] Y.H. Yang, M.Z. Zhang, D.M. Li et al., Simulation study of slow extraction for the Shanghai advanced proton therapy facility. Nucl. Sci. Tech. 28, 120 (2017). doi: 10.1007/s41365-017-0273-0

[8] M.Z. Zhang, D.M. Li, L.R. Shen et al., SAPT: A Synchrotron-Based Proton Therapy Facility in Shanghai. NUCL. INSTRUM. METH. A 34, 148(2023). doi: 10.1007/s41365-023-01293-1

[9] S. Ruan, J.C. Yang, J.W. Xia et al., The 300 MeV proton and heavy ion accelerator complex for SESRI project in China. NUCL. INSTRUM. METH. A 1048, 167916 (2023). doi: 10.1016/j.nima.2022.167916

[10] Z.M. Wang, W. Chen, M.T. Qiu et al., Construction and beam commissioning of a compact proton synchrotron for space radiation environment simulation. NUCL. INSTRUM. METH. A 1027, 166283 (2022). doi: 10.1016/j.nima.2021.166283

[11] W.B. Ye, H.J Yao, S.X. Zheng et al., Analysis and simulation of the tune ripple effect on beam spill ripple in RF-KO slow extraction. Nucl. Sci. Tech. 33, 60 (2022). doi: 10.1007/s41365-022-01038-6

[12] K. Noda, M. Kanazawa, A. Itano et al., Slow beam extraction by a transverse RF field with AM and FM. NUCL. INSTRUM. METH. A 374, 269-277 (1996). doi: 10.1016/0168-9002(96)00096-4

[13] K.Y. Ng, Physics of intensity dependent beam instabilities. (World Scientific, 2006).

[14] Y. Yang, S.X. Zheng, Z.J. Wang et al., Simulation and experiment of low-energy slow extraction at XiPAF, in Proc. IPAC'23, Venice, Italy, May 2023, pp. 2565-2568. doi: 10.18429/JACoW-IPAC2023-TUPM139

[15] Y. Iwata, T. Furukawa, K. Noda et al., Update of an accelerator control system for the new treatment facility at HIMAC, in Proc. of the 11th European Particle Accelerator Conf, Genoa, Italy, 2008, pp.1800-2. Available at https://accelconf.web.cern.ch/e08/papers/tupp118.pdf

[16] Y. Iwata, T. Kadowaki, H. Uchiyama et al., Multiple-energy operation with extended flattops at HIMAC. NUCL. INSTRUM. METH. A 624, 33-38 (2010). doi: 10.1016/j.nima.2010.09.016

[17] K. Mizushima, T. Furukawa, Y. Iwata et al., Performance of the HIMAC beam control system using multiple-energy synchrotron operation. NUCL. INSTRUM. METH. B 406, 347-351 (2017). doi: 10.1016/j.nimb.2017.03.051

[18] K. Mizushima, K. Katagiri, Y. Iwata et al., Experimental studies of systematic multiple-energy operation at HIMAC synchrotron. NUCL. INSTRUM. METH. B 331, 243-247 (2014). 10.1016/j.nimb.2013.12.033

[19] H. Souda, T. Kanai, S.H. Lee et al., Commissioning and first operation of East Japan Heavy Ion Center at Yamagata University. J. PHYS. CONF. SER. 2743, 012092 (2024). doi: 10.1088/1742-6596/2743/1/012092

[20] H. Souda, T. Kanai, S.H. Lee et al., Medical facilities in Japan, in 5th Slow Extraction Workshop, Wiener Neustadt, Austria, 2024. Available at https://indico.gsi.de/event/18184/contributions/76295

[21] J.A. Nelder, R. Mead, A Simplex Method for Function Minimization. COMPUT. J. 7, 308-313 (1965). doi: 10.1093/comjnl/7.4.308

[22] L. Emery, M. Borland, H. Shang, Use of a general-purpose optimization module in accelerator control, in Proceedings of the 2003 Particle Accelerator Conference, Portland, OR, USA, 2003, pp. 2330-2332, vol.4. doi: 10.1109/PAC.2003.1289108

[23] X. Huang, Robust simplex algorithm for online optimization. Phys. Rev. Accel. Beams 21, 104601 (2018). doi: 10.1103/PhysRevAccelBeams.21.104601

[24] A. Scheinker, X. Pang, L. Rybarcy, Model-independent particle accelerator tuning. Phys. Rev. Accel. Beams 16, (2013). doi: 10.1103/PhysRevSTAB.16.102803

[25] A. Scheinker, D. Bohler, S. Tomin et al., Model-independent tuning for maximizing free electron laser pulse energy. Phys. Rev. Accel. Beams. 22, (2019). doi: 10.1103/PhysRevAccelBeams.22.082802

[26] A. Scheinker, X. Huang, J. Wu et al., Minimization of Betatron Oscillations of Electron Beam Injected Into a Time-Varying Lattice via Extremum Seeking. IEEE Trans. Control Syst. Technol. 26, 336-343 (2018). doi: 10.1109/TCST.2017.2664728

[27] X. Huang, J. Corbett, J. Safrane et al., An algorithm for online optimization of accelerators. NUCL. INSTRUM. METH. A 726, 77-83 (2013). doi: 10.1016/j.nima.2013.05.046

[28] Z. Zhang, M. Song, X. Huang, Optimization method to compensate accelerator performance drifts. Phys. Rev. Accel. Beams 25, (2022). doi: 10.1103/PhysRevAccelBeams.25.122801

[29] M. McIntire, T. Cope, S. Ermon et al., Bayesian Optimization of FEL Performance at LCLS, in Proc. IPAC'16, Geneva, Switzerland, June 2016, pp. 2972-2975. doi: 10.18429/JACoW-IPAC2016-WEPOW055

[30] J. Duris, D. Kennedy, A. Hanuka et al., Bayesian Optimization of a Free-Electron Laser. Phys. Rev. Lett. 124, 124801 (2020). doi: 10.1103/PhysRevLett.124.124801

[31] J. Kirschner, M. Nonnenmacher, M. Mutný et al., Bayesian Optimisation for Fast and Safe Parameter Tuning of SwissFEL, in Proceedings of the 39th International Free-Electron Laser Conference, Hamburg, Germany, August 2019, pp. 707-710.

[32] R. Roussel, A. Hanuka, A. Edelen et al., Multiobjective Bayesian optimization for online accelerator tuning. Phys. Rev. Accel. Beams 24, 062801 (2021). doi: 10.1103/PhysRevAccelBeams.24.062801

[33] A. Hanuka, J. Duris, J. Shtalenkova et al., Online tuning and light source control using a physics-informed Gaussian process Adi. arXiv preprint arXiv:1911.01538 (2019).

[34] C. Xu, T. Boltz, A. Mochihashi et al., Bayesian opti-

mization of the beam injection process into a storage ring. Phys. Rev. Accel. Beams 26, 034601 (2023). doi: 10.1103/PhysRevAccelBeams.26.034601

[35] R. Roussel, A.L. Edelen, T. Boltz et al., Bayesian optimization algorithms for accelerator physics. Phys. Rev. Accel. Beams 27, 084801 (2024). doi: 10.1103/PhysRevAccelBeams.27.084801

[36] J. Mockus, On bayesian methods for seeking the extremum, in Optimization Techniques IFIP Technical Conference Novosibirsk, Berlin, Heidelberg, July 1974, pp. 400-404. doi: 10.1007/3-540-07165-2_55

[37] B. Shahriari, K. Swersky, Z. Wang et al., Taking the Human Out of the Loop: A Review of Bayesian Optimization. Proc. IEEE 104, 148-175 (2016). doi: 10.1109/JPROC.2015.2494218

[38] E. Brochu, V.M. Cora, N.D. Freitas, A Tutorial on Bayesian Optimization of Expensive Cost Functions, with Application to Active User Modeling and Hierarchical Reinforcement Learning. arXiv preprint arXiv:1012.2599 (2010).

[39] D.R. Jones, A Taxonomy of Global Optimization Methods Based on Response Surfaces. J. Glob. Optim. 21, 345-383 (2001). doi: 10.1023/A:1012771025575

[40] C.K. Williams, C.E. Rasmussen, Gaussian processes for machine learning. (MIT press Cambridge, MA, 2006), vol. 2.

[41] B. Matérn, Spatial Variation, 2nd edn. Springer-Verlag, 1986.

[42] M.L. Stein, Interpolation of Spatial Data: Some Theory for Kriging. (Springer, 1999).

[43] F. Pedregosa, G. Varoquaux, A. Gramfort et al., Scikit-learn: Machine Learning in Python. J. Mach. Learn. Res. 12, 2825-2830 (2011). doi: 10.5555/1953048.2078195

[44] N. Srinivas, A. Krause, S.M. Kakade et al., Information-Theoretic Regret Bounds for Gaussian Process Optimization in the Bandit Setting. IEEE Trans. Inf. Theory 58, 3250-3265 (2012). doi: 10.1109/TIT.2011.2182033

[45] D.R. Jones, M. Schonlau, W.J. Welch et al., Efficient Global Optimization of Expensive Black-Box Functions. J. Glob. Optim. 13, 455-492 (1998). doi: 10.1023/A:1008306431147

[46] F. Nogueira, Bayesian Optimization: Open source constrained global optimization tool for Python. (2014), https://github.com/fmfn/BayesianOptimization.

[47] P. Virtanen, R. Gommers, T.E. Oliphant et al., SciPy 1.0: Fundamental Algorithms for Scientific Computing in Python. Nat. Methods 17, 261-272 (2020). doi: 10.1038/s41592-019-0686-2

[48] G.R. Li, S.X. Zheng, H.J. Zeng et al., Design and test of an RF acceleration system loaded with magnetic alloy for the proton synchrotron of the Xi'an Proton Application Facility. Nucl. Sci. Tech. 29, 94 (2018). doi: 10.1007/s41365-018-0434-9

[49] H.J. Yao, X. Guan, Y. Li et al., Beam Commissioning of XiPAF Synchrotron, in Proc. IPAC'21, Campinas, SP, Brazil, 2021, pp. 639-642. doi: 10.18429/JACoW-IPAC2021-MOPAB189

[50] Y. Yang, Research on the physics and experiment of low energy slow extraction for proton synchrotron, Ph.D. thesis, Tsinghua University, Beijing, 2022.

[51] Z.J. Wang, H.J. Yao, Y. Yang, Optimization of low-energy slow extraction efficiency of XiPAF. J. PHYS. CONF. SER. 2687, 052033 (2024). doi: 10.1088/1742-6596/2687/5/052033

[52] H.J. Yao, G.R. Li, Q. Zhang et al., in Proc. IPAC'19, Melbourne, Australia, 2019, pp. 3170-3173. doi: 10.18429/JACoW-IPAC2019-WEPTS033

[53] J.E. Younkin, M. Bues, T.T. Sio et al., Multiple energy extraction reduces beam delivery time for a synchrotron-based proton spot-scanning system. Adv. Radiat. Oncol. 3, 412-420 (2018). doi: 10.1016/j.adro.2018.02.006